Available online at www.sciencedirect.com
ScienceDirect
Acta Materialia xxx (2008) xxx–xxx
Acta MATERIALIA
www.elsevier.com/locate/actamat

Microstructure, texture and residual stress in a friction-stir-processed AZ31B magnesium alloy

W. Woo [a,b], H. Choo [a,b,*], M.B. Prime [c], Z. Feng [b], B. Clausen [d]

[a] Department of Materials Science and Engineering, The University of Tennessee, Knoxville, TN 37996, USA
[b] Materials Science and Technology Division, Oak Ridge National Laboratory, Oak Ridge, TN 37831, USA
[c] Analysis and Prediction Group, Los Alamos National Laboratory, Los Alamos, NM 87545, USA
[d] Los Alamos Neutron Science Center, Los Alamos National Laboratory, Los Alamos, NM 87545, USA

Received 22 August 2007; received in revised form 5 December 2007; accepted 7 December 2007

Abstract

Spatial variations of microstructure, hardness, chemical composition, tensile behavior, texture and residual stresses were investigated in a friction-stir-processed (FSP) AZ31B magnesium alloy. The residual stresses were measured using two different methods: neutron diffraction and the contour method. No significant variations in the hardness and chemical compositions were found in the FSP zones, including the severely deformed stir zone (SZ), which showed a finer grain size compared to the heat-affected zone and base material. On the other hand, significant changes in the tensile yield strength, texture, and residual stresses were observed in the FSP zones. The relationship between the texture variations and yield strength reduction; and its influence on the decrease in the residual stress near the SZ is discussed. Finally, the residual stresses measured by neutron diffraction and the contour method are compared and the effect of the texture on neutron diffraction residual stress measurements is discussed.

Keywords: Magnesium alloys; Friction-stir welding; Residual stress; Neutron diffraction; Contour method

1. Introduction

Friction-stir welding (FSW) is a newly developed joining process that has attracted tremendous interest in research and applications due to numerous advantages over traditional fusion welding, including nearly defect-free welds with minimized cracking, fine grain structures and minimized distortion [1]. FSW uses a rotating tool consisting of a threaded pin and shoulder to apply severe plastic deformation and frictional heating to the base metal and produce a strong metallurgical joint, which is achieved in the solid-state during welding [2]. Friction-stir processing (FSP), a variation of FSW, is used to modify the microstructure of materials; examples os such modifications include localized grain refinements and homogenization of precipitate particles [3]. The economic and technological benefits of FSW/FSP have been well recognized in various engineering materials [4].

Magnesium alloys have been receiving significant attention in the transportation industry as lightweight structural materials for energy-efficient vehicles. Various studies have recently been reported on the FSW/FSP of Mg alloys and the topics covered can be classified into three categories: (i) microstructure and hardness [5–12], (ii) texture and fracture [13–15] and (iii) surface modification in metals and composites [16–20].

First, Esparza et al. [5] investigated characteristic grain structures such as the recrystallized stir zone (SZ), transition zone (TZ) and base material (BM) in FSW AZ31B Mg alloy and noted no loss of weld-related strength (based

* Corresponding author. Address: The University of Tennessee, Department of Materials Science and Engineering, 319 Dougherty Engineering Building, Knoxville, TN 37996-2200, USA. Tel.: +1 865 974 3643; fax: +1 865 974 4115.
E-mail address: hchoo@utk.edu (H. Choo).

1359-6454/$34.00 © 2007 Acta Materialia Inc. Published by Elsevier Ltd. All rights reserved.
doi:10.1016/j.actamat.2007.12.020

on microhardness) in the SZ. Later, Chang et al. [6] and Wang et al. [7] reported that the smaller grain size in the SZ did not significantly increase the hardness and suggested a weak grain size dependence in terms of the Hall–Petch relationship in AZ31B Mg alloy. On the other hand, several reports have presented significant hardness decreases in the SZ in the case of initially strain-hardened AZ31B-H24 alloy [9–12]. Secondly, Park et al. [13,14] observed a strong texture development in FSW AZ61 Mg alloy and suggested that the basal plane is roughly aligned with the surface of the tool pin column in the SZ. Woo et al. [15] provided quantitative texture changes using neutron diffraction in FSP AZ31B Mg alloy, which were, in turn, correlated with reduced yield strength and increased elongation along the longitudinal direction in the SZ. The results showed that the integrity and performance of FSW products can be significantly influenced by the texture changes, especially for the Mg alloy, which has a hexagonal close packed (hcp) lattice structure and shows poor workability due to the limited number of available slip systems [21]. Finally, application of the grain-refining capability of FSP to Mg alloys was demonstrated on the highly formable AZ91D Mg alloy [16], Mg-based composites with SiO_2 or SiC reinforced particles [17,18] and AM60B or AZ91 Mg cast alloys [19,20].

The frictional heating and severe plastic deformation involved in FSW/FSP can induce significant residual stresses. The residual stresses in FSW aluminum alloys have been studied extensively – see, for example, Refs. [22–28]. Generally, the maximum tensile residual stresses along the welding direction are measured as ~20–50% of the yield strength of the BM for Al alloys. Furthermore, a recent report [29] showed that the longitudinal residual stress can approach 100% of the yield strength (~300 MPa) of the BM in FSW 304L stainless steel. However, direct experimental investigation of the residual stress in FSW Mg alloys has not been reported.

In this paper, we present: (1) microstructure, hardness, chemical composition and tensile behavior results for the FSP AZ31B Mg alloy; (2) spatially resolved measurements of the texture variations and residual stresses using neutron diffraction and (3) mapping of the residual stresses using the contour method. The spatial variations of the residual stresses, which were measured by the two inherently different techniques, will be compared. Most importantly, we discuss the relationship between the significant texture variations and yield strength reduction and its influence on the residual stress profile in the FSP Mg alloy.

2. Processing, microstructure and mechanical properties

As-received commercial AZ31B Mg alloy plates were used in the hot-rolled and soft-annealed condition (O tempering). The nominal chemical composition (wt.%) was 3.0 Al, 1.0 Zn, 0.2 Mn and the balance Mg. The dimensions of the FSP specimen were $306 \times 306 \times 6.5\ mm^3$ (Fig. 1a). The transverse sides of the plates were clamped to constrain the displacement of the specimen during FSP and the clamping was removed after FSP when the plate was air cooled to 25 °C. The sample was prepared by the "bead-

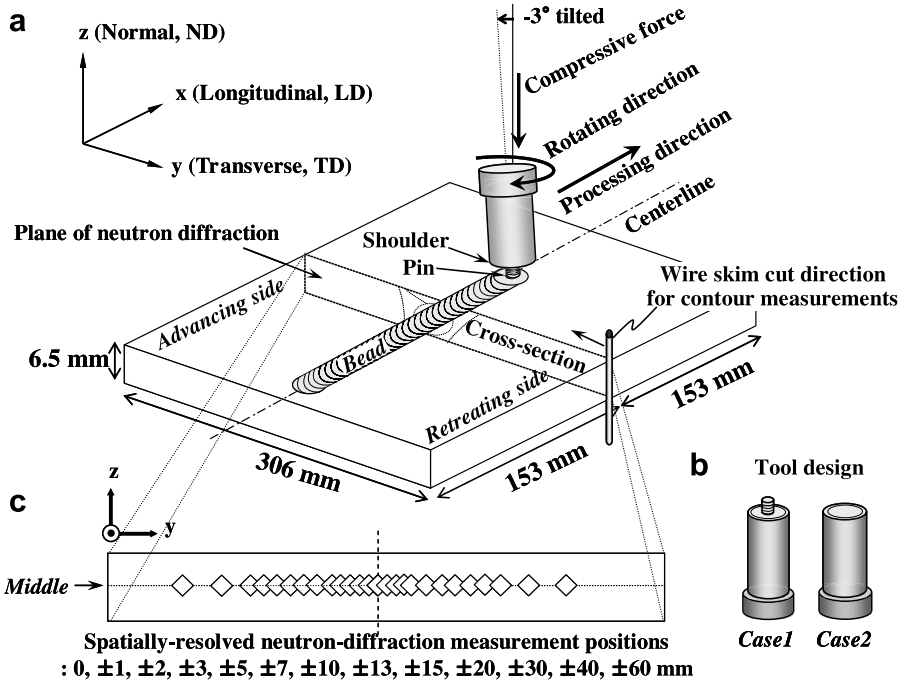

Fig. 1. Schematic of (a) FSP, (b) tool design and (c) spatially resolved neutron diffraction measurement positions across the centerline of the AZ31B magnesium alloy plate.

Please cite this article in press as: Woo W et al., Microstructure, texture and residual stress in a friction-stir-processed ..., Acta Mater (2008), doi:10.1016/j.actamat.2007.12.020

on-plate" method using a single plate instead of joining two pieces of plate.

In order to study the thermal and mechanical effects responsible for the development of the microstructure and stresses during FSP, two FSP cases were examined [25]. A regular FSP plate (Case 1) was processed using both the stirring pin and tool shoulder made of H-13 tool steel and, hence, was subjected to both heating and deformation during FSP. The plate was processed using the following parameters: 0.97 mm s^{-1} traveling speed, 600 r.p.m. clockwise rotating speed and 8000 N compressive force using a tool with a 19.05 mm shoulder diameter and a 6.35 mm pin diameter with a 5.72 mm pin height. The tool was tilted 3° opposite to the processing direction, which coincided with the rolling direction of the BM. Note that the advancing side, where the processing and tool rotating directions are the same, is presented as the negative y-direction (the retreating side is positive) throughout the paper. LD, TD and ND denote longitudinal (x), transverse (y) and normal (z) directions of the plate (Fig. 1a). To minimize the severe plastic deformation and, therefore, isolate thermal effects, a modified FSP plate (Case 2) was processed under the same conditions as Case 1, but utilizing a special tool without the stirring pin (Fig. 1b).

Microstructural characterization was performed at the cross-section (y–z plane) of the FSP plates (Fig. 1a). The samples were cold-mounted, ground, polished and etched with a mixture of 4.2 g picric acid, 10 ml acetic acid, 70 ml ethanol and 10 ml diluted water solution for ~10 s at room temperature for the optical microscopy. Vickers microhardness (H_v) was measured in the "middle" of the plate thickness across the centerline with 1–2 mm horizontal spacing on the polished cross-section using 50 gf applied load (Fig. 1c). Chemical composition analysis was performed along the same line using an energy dispersive spectrometer (EDS). The EDS had a focused electron beam size of 100 × 100 μm with an error range of ±3% for the measured composition. The Mg and Al chemical compositions (wt.%) were measured three times at the same position and averaged.

A total of five tensile specimens were machined at positions of 0, ±10 and ±20 mm from the centerline with the gauge length parallel to the centerline (i.e. longitudinal direction) from both Case 1 and Case 2 plates. The specimens were 6 mm wide, 6.5 mm thick and 25 mm long in the gauge section, following ASTM E 8M-04. In addition, 20 subsize LD tensile samples were prepared from the Case 1 plate; these were 4 mm wide (along ND), 1.65 mm thick (along TD) and 25 mm gauge long (along LD). The subsize samples were cut every 2 mm across the centerline to probe the spatial variation of the longitudinal tensile yield strength in each characteristic region of the FSP plate. All specimens were prepared using electrical-discharge machining (EDM) and tensile tests were performed using a material test system (MTS) load frame with hydraulic wedge-grips at a constant crosshead velocity, providing an initial strain rate of 6.7×10^{-4} s^{-1} at room temperature.

3. Neutron diffraction

3.1. Texture measurement

Neutron diffraction is a well-established technique for spatially resolved measurements of the texture and residual stress inside bulk materials [30,31]. The SMARTS instrument (Spectrometer for MAterials Research at Temperature and Stress) at LANSCE (Los Alamos Neutron Science CEnter) was used for the measurements of texture and residual stress [32]. A line scan was performed at the middle of the plate thickness for both Cases 1 and 2 (Fig. 1c). First, diffraction along the LD and ND were measured simultaneously using a $2(x) \times 2(y) \times 2(z)$ mm^3 scattering volume. Note that 2 mm height (x) and width (z) of incident beam slits and 2 mm radial collimators (y) define the scattering gauge volume. Secondly, the TD and ND diffractions were measured using a scattering volume of $20(x) \times 2(y) \times 2(z)$ mm^3. The intensities of multiple diffractions peaks were analyzed using the single peak fitting (SPF) method in the GSAS general structure analysis system (GSAS) [33] and prismatic $(10\bar{1}0)$ basal (0002) and pyramidal $(10\bar{1}1)$ plane results are presented here.

The integrated intensities (I_τ) of the diffraction peaks provide quantitative insights into the texture variations [30,34]. Specifically, the reduced intensity, which is I_τ divided by λ^4 (wavelength), Z_τ (multiplicity) and $F(\tau)^2$ (structure factor) that vary for each reflection, is proportional to the number of unit cells (N_s) oriented to satisfy Bragg's law within the scattering volume (V_{cell})

$$I_\tau \propto \left(\frac{\lambda^4 Z_\tau F(\tau)^2}{\sin^2\theta}\right)\left(\frac{N_s}{V_{cell}}\right) \quad (1)$$

Thus, the reduced intensity of a specific ($h\ k\ i\ l$) reflection is proportional to the number of unit cells in the scattering volume with their ($h\ k\ i\ l$)-plane normal parallel to the scattering vector. More details can be found in Refs. [34,35].

3.2. Residual stress measurement

Two measurement methods were used to assess residual stresses in the FSP Mg alloy, namely neutron diffraction and the contour method. For the residual stress analysis from the neutron diffraction results, the peak-position changes were analyzed from the same data set described in Section 3.1. Note that the LD, TD and ND were assumed as the three principal directions of the strain tensor in the given plate and that the normal component was measured twice with reasonable reproducibility observed. For the peak analysis, the SPF and Rietveld peak fitting methods were used [33,36]. While the SPF refines each ($h\ k\ i\ l$) reflection, the Rietveld refinement analyzes the entire diffraction profile by comparing the measured and calculated profiles based on the crystallographic space group. The lattice spacings (d_{hkil}) for each ($h\ k\ i\ l$) lattice plane were obtained using the SPF and the lattice parameters

Please cite this article in press as: Woo W et al., Microstructure, texture and residual stress in a friction-stir-processed ..., Acta Mater (2008), doi:10.1016/j.actamat.2007.12.020

for the *a*-axis (a_a) and *c*-axis (a_c) in the hcp structure were analyzed using the Rietveld method.

The residual stress was calculated using a well-established methodology described in elsewhere [22–31,37–39]. Briefly, the residual strain from the SPF can be calculated using $\varepsilon_{hkil} = (d_{hkil}/d^0_{hkil}) - 1$, where d^0_{hkil} is the "stress-free" lattice spacing. A total of ten stress-free reference coupons ($4 \times 4 \times 4\ mm^3$) were machined from the FSP plate (Case 1) at the 0, ±5, ±10, ±15, ±20 and 120 mm positions using EDM. It was assumed that all macroscopic residual stresses in the coupons were fully relaxed and d^0_{hkil} was measured along the LD, TD and ND using a $2(x) \times 2(y) \times 2(z)\ mm^3$ scattering volume. The macroscopic residual stresses were then calculated using the three components of the residual strains by Hooke's law

$$\sigma^{hkil}_{ii} = \frac{E_{hkil}}{1+\nu_{hkil}}\left[\varepsilon^{hkil}_{ii} + \frac{\nu_{hkil}}{1-2\nu_{hkil}}\left(\varepsilon^{hkil}_{xx} + \varepsilon^{hkil}_{yy} + \varepsilon^{hkil}_{zz}\right)\right] \quad (2)$$

where $i = x, y, z$ corresponds to LD, TD and ND, respectively. The elastic constant (E_{hkil}) in any direction of a hexagonal crystal was calculated using the compliance tensors in pure Mg [40]. Note that 45.4 GPa was used for $E_{10\bar{1}1}$ and 0.35 for $\nu_{10\bar{1}1}$ during the SPF analysis. From the Rietveld analysis, the "average" strains were calculated using $\varepsilon^{avg}_{ii} = \left(2\varepsilon^{a}_{ii} + \varepsilon^{c}_{ii}\right)/3$ (combination of the strains along the *a*- and *c*-axes) [41] and *E* (45 GPa) and *v* (0.35) were used for the "average" residual stress calculation.

4. Contour method

The contour method is a newly invented method for determining the residual stress over a cross-section [42]. The displacements of the cut surface (surface contour) due to the relaxation of the residual stress from the cutting are compared to the flat original surface contour to compute analytically the residual stresses using an elastic finite-element (FE) model [43]. The main experimental procedures are: (1) specimen cutting, (2) contour measurement and (3) data reduction and analysis. A detailed description of the general methodology has been published in the literature [27,42–46].

First, the FSP plate (Case 1) was cut in half on the same plane where the neutron diffraction measurements were taken. The cut was made using EDM with a 100 μm diameter brass wire with the part submerged in temperature-controlled deionized water. A "skim cut" setting was used to minimize cutting-induced stresses. A symmetrical clamping arrangement was used to minimize specimen movement as stresses relaxed. Because the part was distorted, high-strength epoxy was used to fill in gaps between the specimen and the clamping plate. The part was cut using a fixed cutting rate of 0.38 mm min^{-1} and took 13.5 h to complete.

After cutting, the contour of the cut surface in each half was measured using a confocal laser probe scanning with a 7 μm diameter spot with ±0.2 μm nominal accuracy [43]. The entire cross-section was mapped using 0.1 and 0.34 mm intervals along TD and ND, respectively

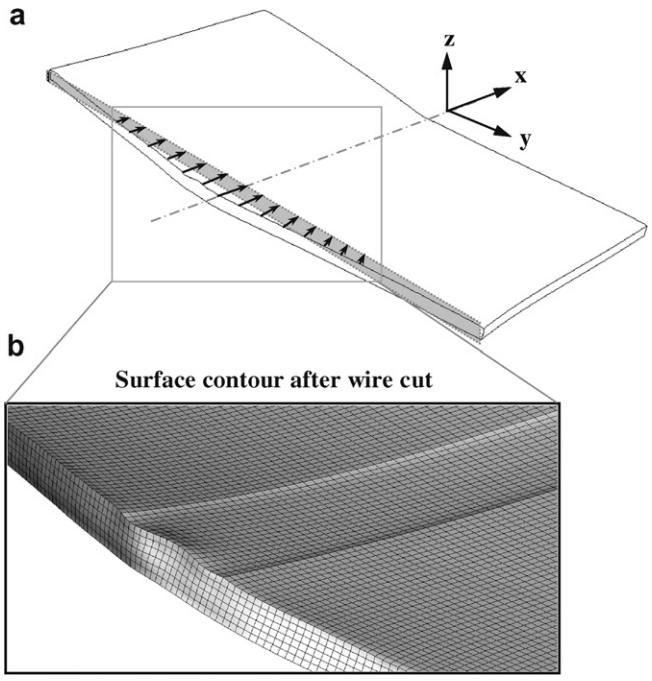

Fig. 2. The contour method: (a) surface contour of the cut surface and (b) surface contour constructed by three-dimensional elastic finite-element model with hexahedral meshes.

(Fig. 2a). The analysis followed published procedures [42]. The contours on the two surfaces were interpolated onto a common grid and then averaged, thus removing any errors caused by shear stresses and the inability to measure transverse displacements.

An ABAQUS 6.5 three-dimensional elastic FE model was constructed for a half-part after the cut. The sample geometry was meshed with 106,248 bi-quadratic (20 node) reduced integration hexahedral elements (Fig 2b). The FE model assumed a homogeneous, isotropic, linearly elastic material with $E = 45$ GPa and $\nu = 0.35$. The signs of the smoothed contour height were reversed to construct the opposite contour and put into the FE model as displacement boundary conditions in the *x*-direction on the cut surface. The transverse displacements on the cut surface were unconstrained, which enforces the condition that the surface is free of shear stress. After the boundary conditions were enforced in an equilibrium analysis step, the normal stress was extracted from the cut surface. The contour method used in this study only determines the stress component normal to the surface of the cut, i.e. σ_{xx}. However, it is worth noting that it is possible to determine other stress components with additional work [47,48].

5. Results

5.1. Microstructure and tensile behavior

The microstructure and texture of the as-received base material (AZ31B-O rolled plate) used in this study have been reported previously [15]. The average grain size was

~50 μm measured by the linear intercept method. The pole figure showed a strong texture, indicating that most of the (0002) basal plane normals were parallel to the ND, which is the typical hot-rolling texture of Mg alloys [13–15]. Fig. 3a shows overall macrostructure of the FSP AZ31B Mg alloy. It shows distinct regions: stir zone (SZ), transition zone (TZ) and heat-affected zone (HAZ). Note that the width of the SZ along the middle was ~8 mm. Fig. 3b clearly shows the significant decreases of the grain size in the SZ (average 17 μm) compared to the BM. The average grain size in the HAZ (87 μm) was, however, larger than that of the BM. Furthermore, there was a significant variation in the grain size through the thickness of the plate (Fig. 3c). A noticeable variation was also found even within a small area (100 × 300 μm^2) marked in the SZ.

Fig. 4 shows microhardness and chemical composition along the middle in the FSP Mg plate. There were no significant spatial variations in hardness or chemical composition after FSP. The hardness results show some scatter (50–70 H_v) (Fig. 4a), but without any noticeable trends. The similarity of hardness in the SZ compared to the BM (58–64 H_v) indicates that there was no significant increase in the microhardness after FSP, even with the grain refinement observed in Fig. 3b. This is consistent with recent studies [6,7] that reported only a weak influence of grain size on hardness changes in FSP AZ31B Mg alloy. Fig. 4b presents the variations of the Mg and Al composition in wt.%. It is evident that there were no pronounced variations in the compositions of Mg (95–96 wt.%) and Al (3.6–4.0 wt.%) compared to those measured in the BM (shown as grey bands).

However, there were significant changes in the tensile behavior after FSP. Fig. 5a shows tensile stress-curves measured using the standard ASTM specimens machined along the LD from the BM and FSP. The BM result shows ~110 MPa longitudinal yield strength (σ_{ys}) and a 32% elongation. The Case 1 results show significantly different tensile behavior compared to that of BM, as well as in between the samples taken at 0 and 10 mm from the centerline. Particularly, the 0 mm sample, which was from the SZ, showed a significant reduction in the σ_{ys} (~55 MPa) and an increased elongation (41%). On the other hand, Case 2 showed similar tensile behavior at these two locations, while showing overall reduction in the σ_{ys} compared to the BM. Fig. 5b shows the ratio of the tensile σ_{ys} between FSP and BM as a function of distance from the centerline. For Case 1, at ±30 mm the σ_{ys} was ~70% of the BM, approaching the centerline it increased to >90%, but right at the centerline it sharply decreased to ~50% of the BM. The significant decrease at 0 mm in the subsize sample is consistent with the result from the standard tensile specimen. In contrast, the tensile results did not show the significant reduction across the centerline in Case 2.

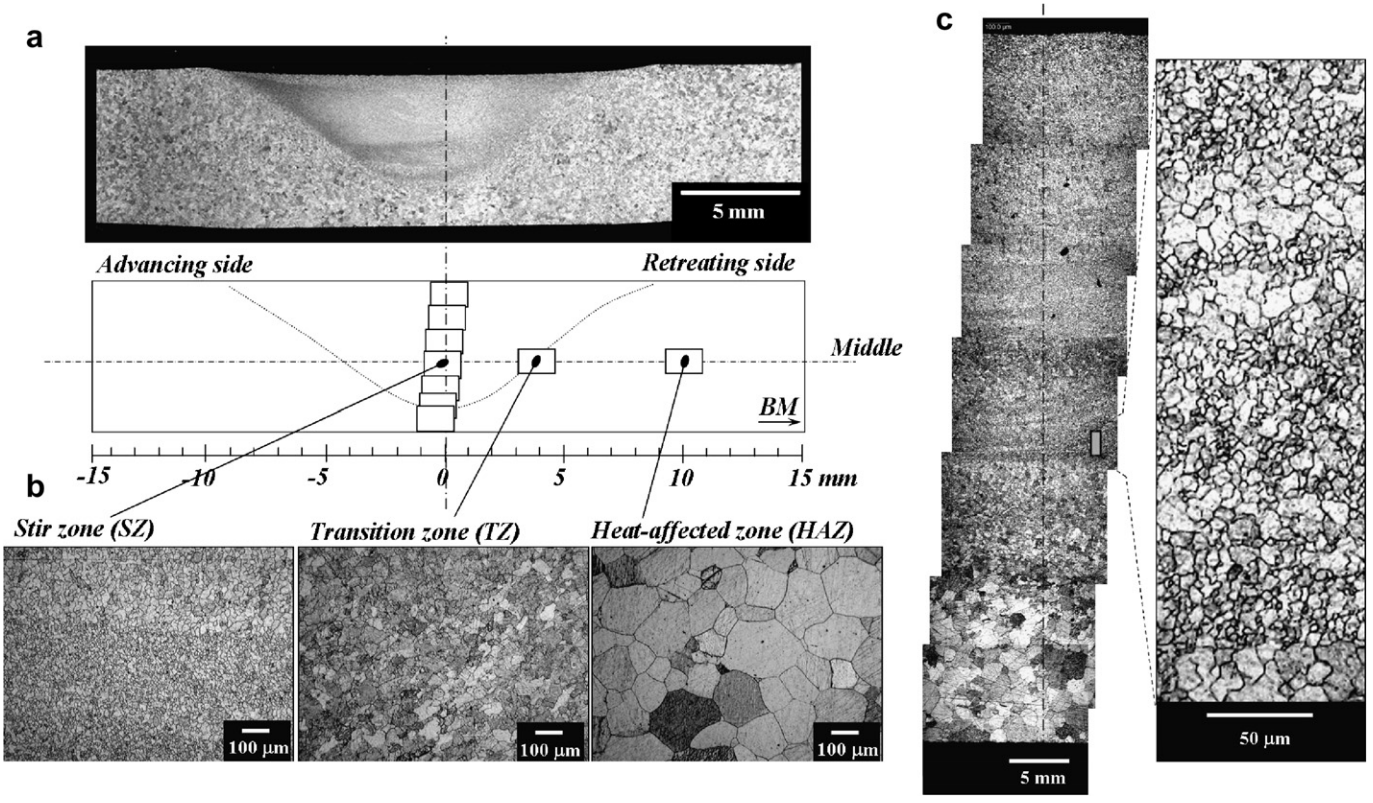

Fig. 3. Optical micrographs of the FSP AZ31B Mg alloy: (a) overall cross-sectional macrostructure; (b) microstructure of the SZ, TZ and HAZ; and (c) microstructure through the thickness of the plate along the centerline. Significant variations of the grain size were observed (i) across the SZ, TZ and HAZ, (ii) through the thickness and (iii) even within the SZ (e.g. 100 × 300 μm^2 region marked with a square in c).

Please cite this article in press as: Woo W et al., Microstructure, texture and residual stress in a friction-stir-processed ..., Acta Mater (2008), doi:10.1016/j.actamat.2007.12.020

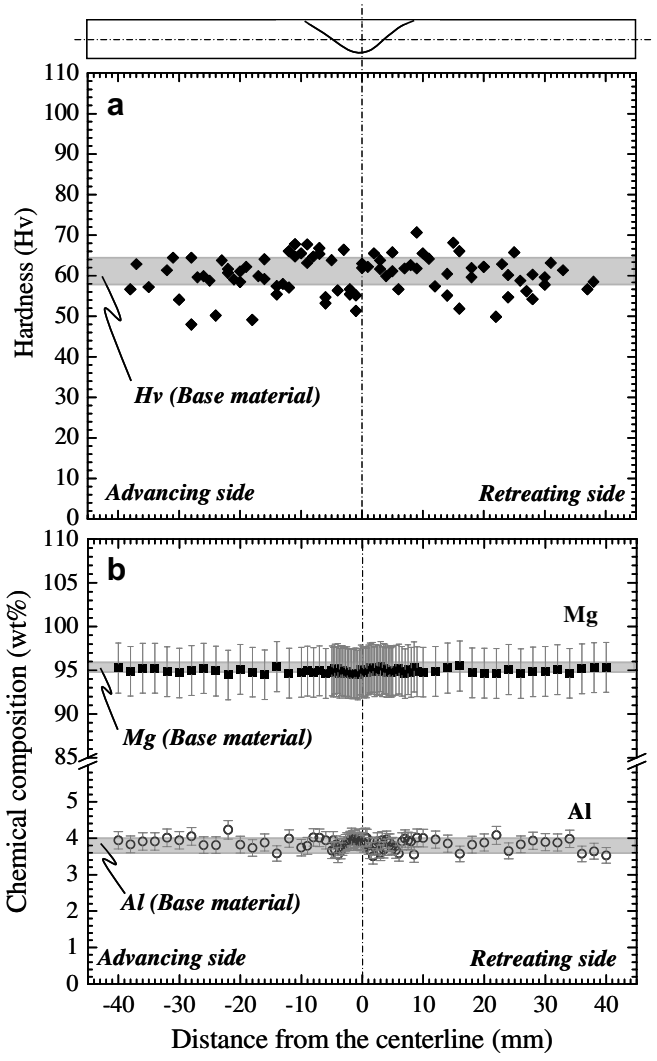

Fig. 4. (a) Microhardness and (b) chemical composition measured along the middle of the FSP AZ31B Mg alloy. The results show no significant variations as a function of distance from the centerline. The properties measured from the BM are shown as a thin grey band for comparison.

5.2. Texture variations after FSP

Fig. 6 shows the variations of the reduced peak intensities of the prismatic $(10\bar{1}0)$ basal (0002) and pyramidal $(10\bar{1}1)$ planes along the LD, TD and ND across the centerline in Cases 1 and 2. The fundamental basis and the usefulness of the reduced intensities in describing the spatial variation of the texture in FSP plate, along with the comparison to full pole figures, have been reported previously in the case of an FSP Al alloy [35]. First, the reduced intensity of a particular (*h k i l*) reflection provides quantitative insights into the texture variation. Let us consider (0002) in Case 1 (Fig. 6b). It showed a reduced intensity of 1.4 for the (0002) peak along the ND and 0.2 along the TD at the −60 mm position. This indicates that there are approximately seven times more unit cells with their (0002) plane normal oriented to ND than TD in BM. The relative ratio is comparable to the pole density ratio (previously measured as 7.4) in the (0002) pole figure of the BM reported in Ref. [15].

Secondly, the reduced intensities in the SZ of Case 1 were significantly different compared to the BM or HAZ (Fig. 6a–c). Most notably, Fig. 6b shows that the 1.4 reduced intensity along ND at −60 mm increased up to 2.3 at −20 mm and significantly decreased to 0.7 at 0 mm. Furthermore, the TD and ND reduced intensity variations suggest that the basal plane normal was mainly parallel to the ND at BM/HAZ, mostly parallel to the TD near the TZ and not parallel to either ND or TD in the SZ (Fig. 6b). On the other hand, the reduced intensity profiles in Case 2 do not show such significant variations near the SZ (Fig. 6d–f). Although there are visible changes at 8–12 mm of the (0002) reflection (Fig. 6e), the change was not nearly as significant as Case 1 and the prismatic or pyramidal reflections showed very little change. Moreover, the full pole figure measured at 8–12 mm position showed that the texture was similar to the BM (not shown here). Thus, the variation of the reduced intensity (texture) was significant in the SZ in Case 1, while almost no variation was observed in Case 2. The "presence" of each reflection in the diffraction profile measured in each orientation is summarized in Table 1 and the implications of "missing reflections" on the stress analysis will be discussed in Section 6.2.

5.3. Residual stress in the FSP Mg plate

Fig. 7 shows the residual stresses measured by neutron diffraction using both the SPF and Rietveld methods in the FSP Mg plate (Cases 1 and 2). Since only the pyramidal $(10\bar{1}1)$ peak exhibited sufficient intensities along all three directions, as shown in Table 1, the longitudinal (σ_{xx}), transverse (σ_{yy}) and normal (σ_{zz}) residual stresses were calculated using the $(10\bar{1}1)$ data (Fig. 7a). A peak-and-valley shape is evident, such as has been seen in FSP Al alloys [22–28]. For example, σ_{xx} shows compressive stress (−40 MPa) at −60 mm, increases to maximum tensile stress (135 MPa) at ±2 mm and sharply decreases to compressive stress (−10 MPa) around 0 mm. The changes are qualitatively similar for σ_{yy} and σ_{zz}. Fig. 7b shows the residual stresses obtained using the Rietveld method. The absence of the data points within the ±2 mm region is due to the insufficient peak intensity of certain reflections resulting from the texture distributions in the SZ. Overall, the residual stress determined using the Rietveld method is in good agreement with the SPF results. Fig. 7c–d shows the residual stress profiles obtained in Case 2. Note that the lattice spacing measured at −60 mm of the plate was used as the "stress-free" lattice spacing. As for Case 1, the results for Case 2 are in good agreement between the two methods. However, contrary to Case 1, the results for Case 2 do not show the sharp decrease in the residual stress near the SZ. More detailed discussion will be presented in Section 6.1.

Please cite this article in press as: Woo W et al., Microstructure, texture and residual stress in a friction-stir-processed ..., Acta Mater (2008), doi:10.1016/j.actamat.2007.12.020

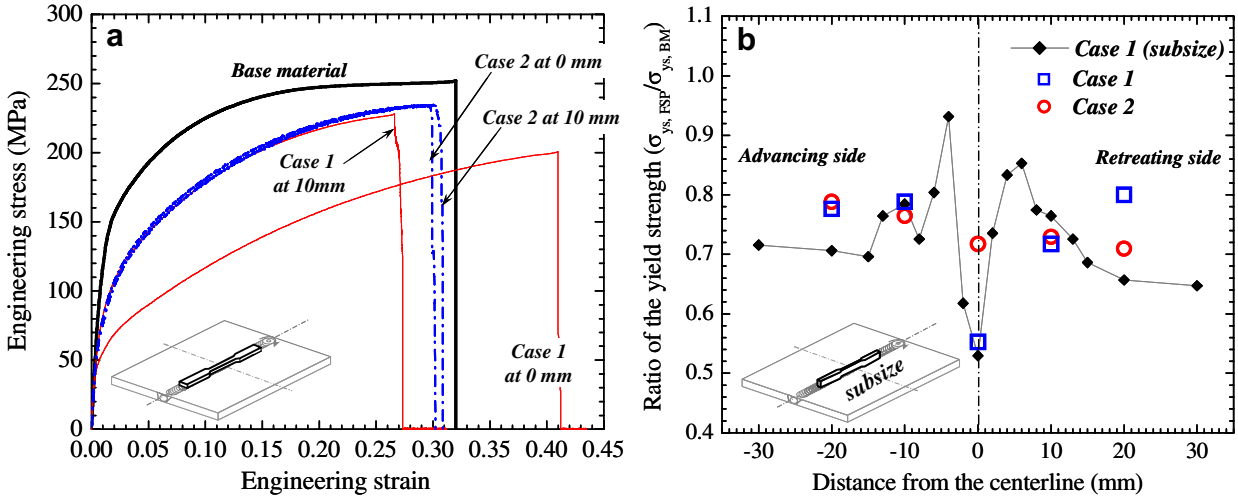

Fig. 5. Tensile test results measured along the longitudinal direction (LD) of AZ31B Mg alloy: (a) tensile stress–strain curves of the BM, Case 1 (at 0 and 10 mm) and Case 2 (at 0 and 10 mm) and (b) the ratio of the tensile yield strength (σ_{ys}) between FSP and BM as a function of distance from the centerline. The results from the standard tensile specimens are shown as open squares for Case 1 and open circles for Case 2. The results from the subsize specimens for Case 1 are also shown (solid diamonds), with a better spatial resolution depicting a clear variation of the longitudinal σ_{ys} across the centerline.

Fig. 8 shows the results from the contour method showing the σ_{xx} measured for the FSP Mg alloy (Case 1). The measured displacement contour (~200 μm variation) was converted to stress following the steps of data analysis described in Section 4. Note that the thickness of the plate is magnified by a factor of three for clarity (Fig. 8a). Significant tensile stresses are observed at ±10 mm and mild compressive stresses further away from the centerline for the required stress balance. Fig. 8b shows the σ_{xx} profile extracted along the three marked lines and averaged to make it comparable to the sampling volume of the neutron diffraction measurements. The σ_{xx} profile slows ~−30 MPa at ±150 mm and a maximum of ~90 MPa at −7 mm, with a sharp drop to ~20 MPa at the centerline. It is important to note that the significant decrease in the residual stress (~70 MPa) from −7 to 0 mm is consistent with the result of the neutron diffraction for Case 1 obtained using the SPF method, as shown in Fig. 7a. For the comparison, the longitudinal residual stress (σ_{xx}) obtained from the neutron diffraction (both SPF and Rietveld) and the contour method are plotted in Fig. 9, which show a good agreement.

6. Discussion

6.1. Residual stress in FSP Mg alloy

The influence of the severe plastic deformation during FSP on the texture development and its effect on the longitudinal yield strength (σ_{ys}) will be discussed in this section. Furthermore, the relationship between the σ_{ys} reduction and the reduction of the residual stress will be discussed by contrasting the different experimental observations from Cases 1 and 2.

The general trends of the residual stress profiles are similar between Case 1 (tool pin and shoulder) and Case 2 (tool shoulder only) in the FSP AZ31B Mg alloy (Fig. 7). This suggests that the dominant source of the residual stress was the frictional heating from the tool shoulder, as established for the case of an Al alloy [25]. More interestingly, the results in Case 1 show a sharp decrease in the residual stress near the SZ, unlike Case 2 (Figs. 7 and 8). For FSP Al alloys, it has previously been reported that the reduction in the residual stress profile observed near the centerline is due to the σ_{ys} reduction resulting from the microstructural softenening (e.g. dissolution and coarsening of strengthening precipitates) caused by the frictional heating, mainly from the tool shoulder [24,25,28]. Therefore, the softening effect was observed in both Cases 1 and 2 of the FSP Al alloy [25,28]. However, in the case of FSP Mg alloy, the softening was observed only in Case 1. Furthermore, compared to the residual stress profiles of FSP Al alloys [22–28], the softening near the centerline is quite distinct in the FSP Mg alloy (Case 1). It is suggested that the severe plastic deformation from the tool pin, rather than the frictional heating from the tool shoulder, caused the texture changes in FSP [35]. The shear plastic flow associated with the severe plastic deformation, which is caused by the tool pin during FSP, creates crystallographic rearrangements of the basal (0002) plane (preferential slip plane) in that the basal planes surround the tool pin surface in the SZ [13–15]. As a result, significant texture changes were clearly observed in the SZ of the FSP Mg alloy (Case 1) (Fig. 6a–c), while little change was observed in Case 2 (Fig. 6d–f). Since the basal plane in the Mg alloy is neither parallel nor perpendicular to the tensile direction (LD) in the SZ, the FSP texture near the SZ causes the increases in Schmid factor and lower σ_{ys} in the SZ compared to the BM or HAZ [15]. The effect of severe plastic deformation on the texture variation and, in turn, on the σ_{ys} is clearly manifested in Figs. 5 and 6a–c for Case 1. In contrast, the nearly constant σ_{ys} in Case 2 across the centerline is well-correlated to the fact that there was almost no tex-

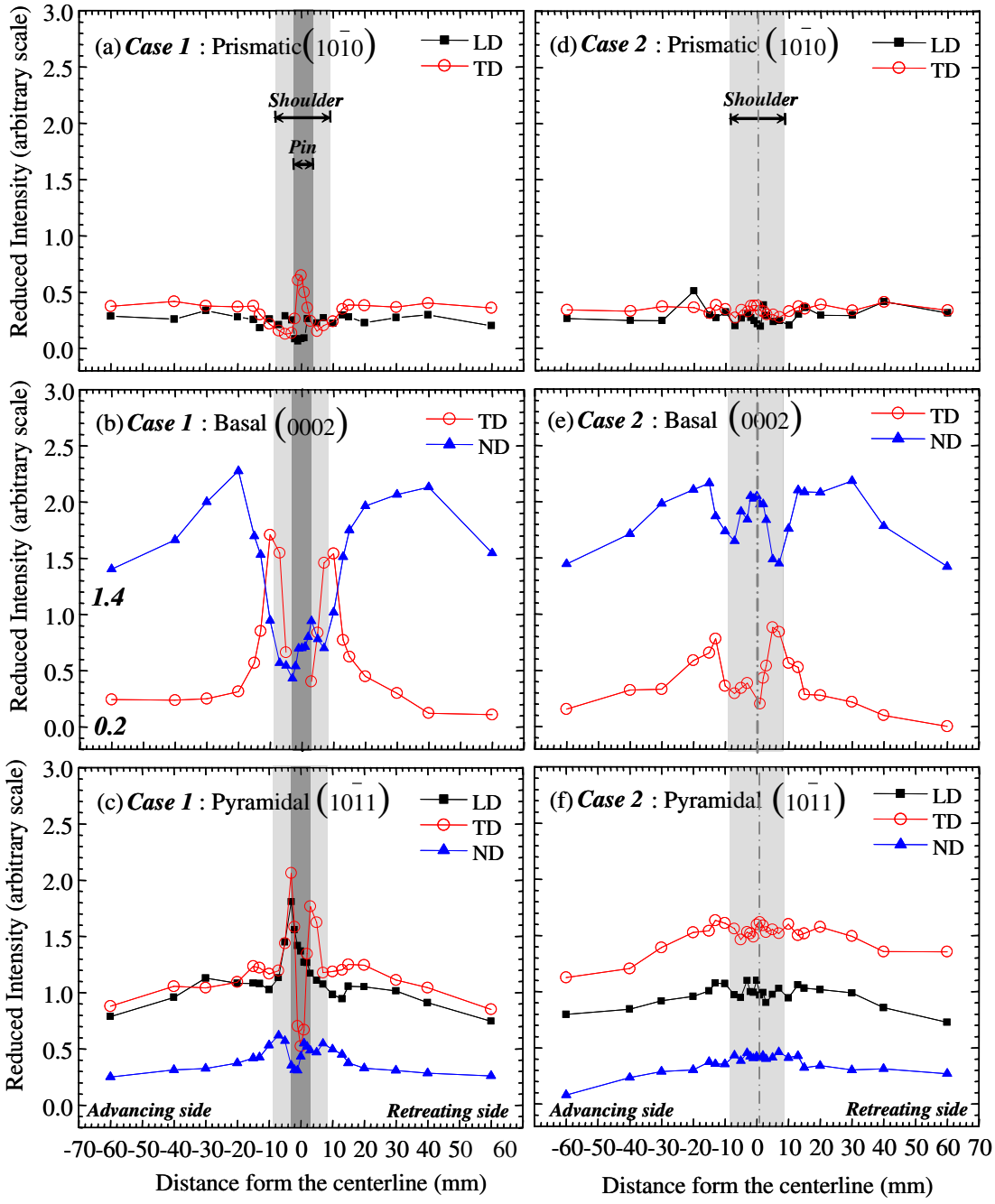

Fig. 6. The reduced intensities of the prismatic $(10\bar{1}0)$, basal (0002) and pyramidal $(10\bar{1}1)$ reflections measured along the middle of the plate thickness across the centerline, with their scattering vectors parallel to the longitudinal (LD), transverse (TD) and normal directions (ND): (a) $(10\bar{1}0)$, (b) (0002) and (c) $(10\bar{1}1)$ from Case 1; (d) $(10\bar{1}0)$, (e) (0002) and (f) $(10\bar{1}1)$ from Case 2.

ture change in Case 2 (Figs. 5 and 6d–f). It is worth noting that the hardening behavior is similar for all cases (Fig. 5a), whereas the flow-stress is significantly lower for Case 1 at 0 (mainly due to the lower yield stress), indicating that the Taylor factor, M, also varies as a function of position within the FSP Mg alloy [49].

Consequently, texture-induced σ_{ys} reduction could be the main cause for the residual stress reduction near the SZ observed in Case 1. The σ_{ys} profile obtained using the subsize tensile specimens (Fig. 5b), is qualitatively similar to the residual stress profile (Figs. 7a and 8b). The relationship between σ_{ys} and residual stress is more evident when comparing the results between Cases 1 and 2. The clear decreases in the residual stress of the SZ in Case 1 cannot be found in Case 2, which does not show this σ_{ys} reduction. In summary, the severe plastic deformation caused by the tool pin caused significant texture variation across the centerline in Case 1, which resulted in an increase in Schmid factor and a reduction in the longitudinal σ_{ys} near the SZ. As a consequence,

Please cite this article in press as: Woo W et al., Microstructure, texture and residual stress in a friction-stir-processed ..., Acta Mater (2008), doi:10.1016/j.actamat.2007.12.020

Table 1
The results of SPF analysis of the diffraction profiles summarizing the presence of the prismatic $(10\bar{1}0)$ basal (0002) and pyramidal $(10\bar{1}1)$ planes along the LD, TD and ND in Cases 1 and 2

Peak	LD	TD	ND
$(10\bar{1}0)$ Prismatic	O	O	X
(0002) Basal	X	O[a]	O
$(10\bar{1}1)$ Pyramidal	O	O	O

"O" indicates that the reflection was available and "X" denotes that the reflection was missing or of poor quality, unsuitable for analysis due to the texture. The missing reflections were the $(10\bar{1}0)$ peak along ND, the (0002) peak along LD and the (0002) peak along TD within ±2 mm of Case 1 due to the strong texture of the BM and FSP Mg alloy. Note that only the $(10\bar{1}1)$ peak was available along all three directions, allowing the residual stress calculation.

[a] Note that the (0002) reflection along TD is missing within ±2 mm in Case 1.

the residual stress profile of Case 1 exhibits a sharp decrease in the SZ due to localized texture-induced softening, which was not observed in Case 2.

Finally, the decrease in σ_{ys} near the SZ in Case 1, in spite of no corresponding decreases in hardness (Fig. 4a), implies that the microhardness does not represent the macroscopic tensile properties in the current case where the texture change is responsible for the softening rather than the dissolution or growth of precipitates in the case of, for example, FSP Al 6061-T6 alloy. In addition, since nearly constant chemical composition was observed in the SZ, HAZ and BM (Fig. 4b), the presence or dissolution of a new phase or compound is not plausible as an explanation of the changes in σ_{ys}.

6.2. Effect of texture on the residual stress measurements

Neutron diffraction stress measurement is tricky when the material has a strong texture, large grain size, or inhomogeneous chemical composition [37,39,50]. Mg alloy plate exhibits a strong texture and the SPF results showed insufficient peak intensities from certain specific (*h k i l*) planes along certain directions, as summarized in Table 1. For example, the (0002) basal plane normal is predominantly oriented to the ND/TD in the BM (Fig. 6b). Similarly, the missing (0002) diffraction peak within the SZ along TD (Fig. 6b), which is caused by the strong texture distribution (e.g. basal plane surrounding the pin column) in the FSP Mg alloy, is problematic for stress analysis.

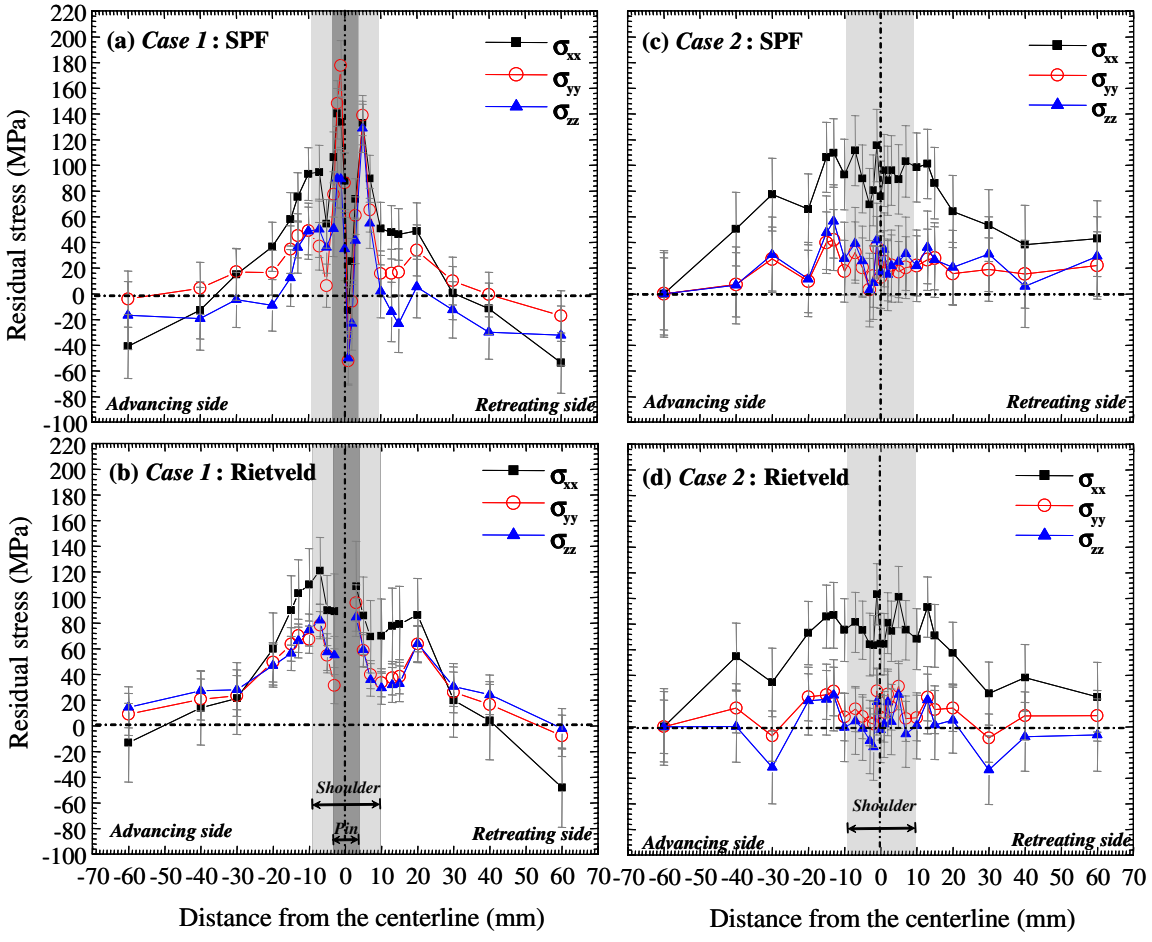

Fig. 7. Residual stresses in the FSP AZ31B Mg alloy. Longitudinal (σ_{xx}), transverse (σ_{yy}) and normal (σ_{zz}) stresses were measured using neutron diffraction and analyzed using: (a) SPF of $(10\bar{1}1)$ for Case 1; (b) Rietveld refinement for Case 1; (c) SPF of $(10\bar{1}1)$ for Case 2; and (d) Rietveld refinement for Case 2. Residual stresses from the Rietveld method within ±2 mm of Case 1 are not available due to a strong texture within the SZ.

Please cite this article in press as: Woo W et al., Microstructure, texture and residual stress in a friction-stir-processed ..., Acta Mater (2008), doi:10.1016/j.actamat.2007.12.020

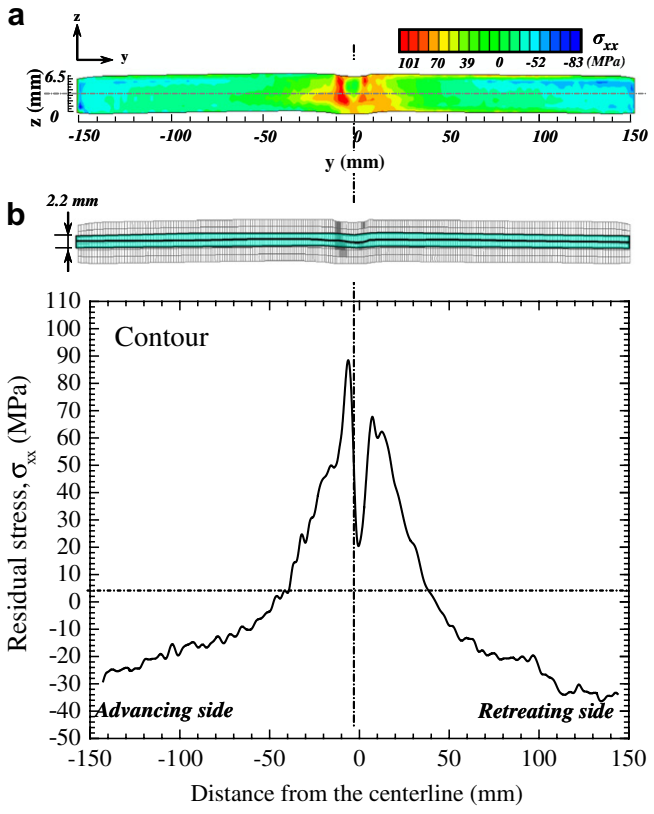

Fig. 8. Longitudinal residual stress (σ_{xx}) measured using the contour method for Case 1: (a) cross-sectional contour map of σ_{xx} on the y–z plane shown in Fig. 1 and (b) σ_{xx} variation as a function of distance from the centerline. The σ_{xx} profile is the average over the three lines across the centerline at $z = 3.25$ and 3.25 ± 1.1 mm, following the nodes in the mesh of the finite-element modeling.

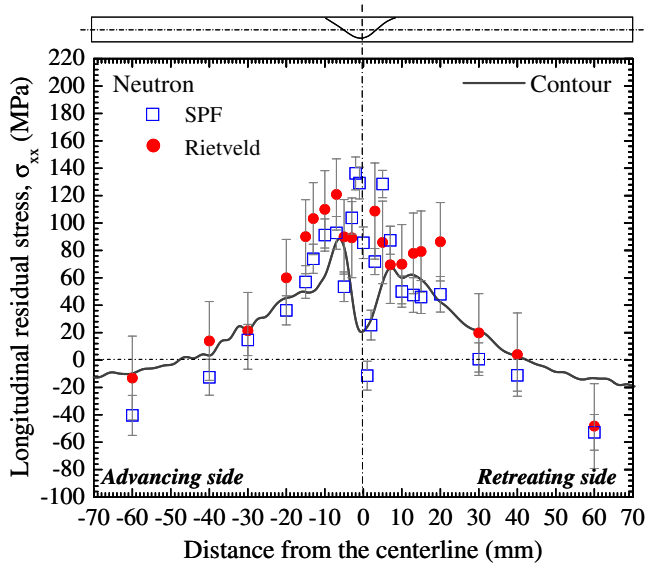

Fig. 9. Comparison between the longitudinal residual stresses (σ_{xx}) measured using the contour method and neutron diffraction. The diffraction data include SPF (pyramidal peak) and Rietveld results.

However, since the $(10\bar{1}1)$ pyramidal diffraction peak was available along LD, TD and ND (Fig. 6c), it was used to calculate residual stresses in FSP plate (Fig. 7a).

The different stress analysis can also provide an erroneous result within the SZ due to the strong texture (Fig. 7b). For example, the sharp changes in texture across the SZ in the FSP Mg alloy can cause an inhomogeneous distribution of a certain diffraction plane within the scattering volume. This could cause a mismatch between the geometric centroid of the nominally defined neutron gauge volume and the centroid of the actually "sampled" gauge volume and so could result in an artificial shift in the measured d-spacing and errors in the measured strains. Such an effect (often called an "edge effect") is often encountered when the neutron gauge volume is only partially filled with the specimen during measurement of stresses near the specimen surface [39,51]. Therefore, the contour method result was essential to eliminate the ambiguities in interpreting the neutron diffraction results due to the texture effect in FSP Mg alloy. Indeed, the contour method result clearly showed the significant decreases in the macroscopic σ_{xx} within the SZ (Fig. 9). Furthermore, the comparison shows a good agreement within experimental uncertainties. For example, the peak at -7 mm was $\sim 90 \pm 5.0$ MPa using the contour method and 93 ± 12 MPa (SPF) and 120 ± 26 MPa (Rietveld) using neutron diffraction. Furthermore, the asymmetric distributions of the residual stress between the advancing and retreating sides was similarly evident in both measurements.

7. Conclusions

1. Microstructure, hardness and chemical composition were examined in an FSP AZ31B Mg alloy. In spite of the refined grain size, no significant variations in the hardness or chemical composition were found in the severely deformed SZ compared to the HAZ and BM.
2. The longitudinal tensile behavior was investigated using tensile specimens machined along the longitudinal direction from: (i) BM, (ii) typical FSP plate (Case 1, processed using a regular tool with a pin and shoulder) and (iii) modified FSP plate (Case 2, processed with a tool with shoulder only to minimize plasticity-induced effects caused by the pin). There were significant yield strength reductions (55% of the BM) in the SZ of Case 1, while this was not observed in Case 2.
3. Spatial texture variation as a function of distance from the FSP centerline was measured using neutron diffraction in Cases 1 and 2. The variation of the reduced peak intensity (texture) was analyzed using the prismatic $(10\bar{1}0)$ basal (0002) and pyramidal $(10\bar{1}1)$ reflections and it showed a significant variation in the SZ in Case 1, while almost no variation was observed in Case 2.
4. Residual stresses were measured using neutron diffraction and the contour method. The neutron diffraction results were analyzed using both the single peak fitting (SPF) and Rietveld methods for the FSP Mg plate (Cases 1 and 2). For neutron diffraction results, the residual stress profiles show significant decreases near the SZ (± 2 mm) in Case 1, while this was not observed

in Case 2. The contour method result was consistent with the neutron diffraction results for Case 1 and it also clearly showed the significant decreases in the residual stress (up to 70 MPa) near the SZ.

5. Overall, similar residual stress profiles were observed in both Cases 1 and 2, suggesting that the dominant source of the residual stress is frictional heating from the tool shoulder. On the other hand, near the SZ, a sharp decrease in residual stress was observed only in Case 1, which suggests that this decrease is related to the severe plastic deformation rather than the frictional heat. The severe plastic deformation caused significant texture variation in Case 1, which resulted in an increase in Schmid factor and reduction in the longitudinal σ_{ys} near the SZ. As a result, the residual stress profile of Case 1 exhibits a sharp decrease in the SZ due to localized texture-induced softening, which was not observed in Case 2.

Acknowledgements

This work was supported by the NSF International Materials Institutes (IMI) Program under contract DMR-0231320. This work has benefited from the use of the Los Alamos Neutron Science Center at the Los Alamos National Laboratory, operated by Los Alamos National Security LLC for the National Nuclear Security Administration of the US Department of Energy under contract DE-AC52-06NA25396. This research was also sponsored by the Laboratory Directed Research and Development Program of Oak Ridge National Laboratory (ORNL), managed by UT-Battelle LLC for the US Department of Energy under Contract No. DE-AC05-00OR22725. The authors would like to thank S.R. Agnew and D.W. Brown for helpful discussions and A. Frederick, T. Sisneros and G. Wang for their help during experiments.

References

[1] Thomas WM, Nicholas ED, Needham JC, Murch MG, Templesmith P, Dawes CJ. International Patent PCT/GB92/02203, GB Patent 9125978.8; 1991, US Patent 5,460,317 1995.
[2] Mahoney MW, Rhodes CG, Flintoff JG, Spurling RA, Bingle WH. Metal Mater Trans A 1998;29A:1955.
[3] Berbon PB, Bingel WH, Mishra RS, Bampton CC, Mahoney MW. Scripta Mater 2001;44:61.
[4] Mishra RS, MA ZY. Mater Sci Eng R 2005;50:1–78.
[5] Esparza JA, Davis WC, Trillo EA, Murr LE. J Mater Sci Lett 2002;21:917–20.
[6] Chang CI, Lee CJ, Huang JC. Scripta Mater 2004;51:509–14.
[7] Wang YN, Chang CI, Lee CJ, Lin HK, Huang JC. Scripta Mater 2006;55:637–40.
[8] Wang X, Wang K. Mater Sci Eng A 2006;431:114–7.
[9] Lee WB, Yeon YM, Jung SB. Mater Sci Technol 2003;19:785–90.
[10] Somasekharan AC, Murr LE. Mater Charact 2004;52:49–64.
[11] Lim S, Kim S, Lee C, Yim CD, Kim SJ. Metal Mater Trans A 2005;34:1609–12.
[12] Afrin N, Chen DL, Cao X, Janazi M. Mater Sci Eng A 2008;472:179–86.
[13] Park SHC, Sato YS, Kokawa H. Metall Mater Trans A 2003;34:987–94.
[14] Park SHC, Sato YS, Kokawa H. Scripta Mater 2003;49:161–6.
[15] Woo W, Choo H, Brown DW, Feng Z, Liaw PK. Scripta Mater 2006;54:1859–64.
[16] Sato YS, Park SHC, Matsunaga A, Honda A, Kokawa H. J Mater Sci 2005;40:637–42.
[17] Lee CJ, Huang JC, Hsieh PJ. Scripta Mater 2006;54:1415–20.
[18] Morisada Y, Fujii H, Nagaoka T, Fukusumi M. Mater Sci Eng A 2006;433:50–4.
[19] Santella M, Frederick A, Degen C, Pan TY. JOM 2006;58:56–61.
[20] Feng AH, Ma ZY. Scripta Mater 2007;56:397–400.
[21] ASM International. ASM speciality handbook: magnesium and magnesium alloys. Materials Park, OH: ASM International; 1999.
[22] Sutton MA, Reynolds AP, Wang DQ, Hubbard CR. J Eng Mater Technol 2002;124:215–21.
[23] Staron P, Kocak M, Williams S. Appl Phys A 2002;74:S1161–2.
[24] Peel M, Steuwer A, Preuss M, Withers PJ. Acta Mater 2003;51:4791–801.
[25] Woo W, Choo H, Brown DW, Feng Z, Liaw PK, David SA, Hubbard CR, Bourke MAM. Appl Phys Lett 2005;86:231902.
[26] Woo W, Choo H, Brown DW, Feng Z, Liaw PK. Mater Sci Eng A 2006;437:64–9.
[27] Prime MB, Gnaupel-Herold T, Baumann JA, Lederich RJ, Bowden DM, Sebring RJ. Acta Mater 2006;54:4013–21.
[28] Woo W, Choo H, Brown DW, Feng Z. Metall Mater Trans A 2007;38:69–76.
[29] Reynolds AP, Tang W, Gnaupel-Herold T, Prask H. Scripta Mater 2003;48:1289–94.
[30] Windsor CG. Pulsed neutron scattering. London: Taylor and Francis; 1981.
[31] Allen AJ, Hutchings MT, Windsor CG, Andreani C. Adv Phys 1985;34:445–73.
[32] Bourke MAM, Dunand DC, Ustundag E. Appl Phys A 2002;74:S1707–9.
[33] Larsen AC, Von Dreele RB. General Structure Analysis System, GSAS, LAUR 86-748. Los Alamos National Laboratory, Los Alamos, NM, 2004.
[34] Carr DG, Ripley MI, Holden TM, Brown DW, Vogel SC. Acta Mater 2004;52:4083–91.
[35] Woo W, Choo H, Brown DW, Feng Z, Liaw PK, Vogel SC. Acta Mater 2006;54:3871–82.
[36] Rietveld HM. Acta Cryst 1967;22:151–2.
[37] Holden TM, Suzuki H, Carr DG, Ripley MI, Clausen B. Mater Sci Eng A 2006;437:33–7.
[38] Choo H, Bourke M, Nash P, Daymond M, Shi N. Mater Sci Eng A 1999;264:108–21.
[39] Hutchings MT, Withers PJ, Holden TM, Lorentzen T. Introduction to the characterization of residual stress by neutron diffraction. Boca Raton, FL: Taylor & Francis; 2005.
[40] Kelly A, Groves GW. Crystallography and crystal defects. London: Longman; 1970.
[41] Daymond MR, Bourke MAM, Von Dreele RB. J App Phys 1999;85:739–47.
[42] Prime MB. J Eng Mater Technol 2001;123:162–8.
[43] Prime MB, Sebring RJ, Edwards JM, Hughes DJ, Webster PJ. Exp Mech 2004;44:176–84.
[44] Zhang Y, Ganguly S, Edwards L, Fitzpatrick ME. Acta Mater 2004;52:5225–32.
[45] DeWald AT, Rankin JE, Hill MR, Lee MJ, Chen HL. J Eng Mater Technol 2004;126:465–73.
[46] Kartal M, Turski M, Johnson G, Fitzpatrick ME, Gungor S, Withers PJ, et al. Mater Sci Forum 2006;524–525:671–6.
[47] DeWald AT, Hill MR. Exp Mech 2006;46:473–90.
[48] Korsunsky AM, Regino GM, Nowell D. Int J Solids Struct 2007;44:4574–91.
[49] Taylor GI. J Inst Metals 1938;62:307–24.
[50] Steuwer A, Dumont M, Peel M, Preuss M, Withers PJ. Acta Mater 2007;55:4111–20.
[51] Spooner S, Wang XL. J Appl Cryst 1997;30:449–55.